JGR Solid Earth

RESEARCH ARTICLE
10.1029/2023JB027510

Special Section:
Solid Earth Geophysics as a means to address issues of global change

Experimental Study of the Generation of Pore Gas Pressure in Pyroclastic Density Currents Resulting From Eruptive Fountain Collapse

Baptiste Penlou[1], Olivier Roche[1], and Siet van den Wildenberg[1,2]

[1]Laboratoire Magmas et Volcans, CNRS, IRD, OPGC, Université Clermont Auvergne, Clermont-Ferrand, France, [2]Laboratoire de Physique de Clermont, CNRS/IN2P3, Université Clermont Auvergne, Clermont-Ferrand, France

Abstract Pyroclastic density currents formed through collapse of eruptive fountains commonly have runout distances of the order of tens of kilometers. A possible cause of this high flow mobility is elevated interstitial pore gas pressure, which may have various origins. We investigated experimentally the generation of pore pressure at the impact zone of an eruptive fountain, where concentrated pyroclastic density currents emerge from compaction of a free falling gas-particle mixture. We simulated pyroclastic fountain collapse by releasing glass beads of mean sizes of 29–269 μm from a hopper at height of 3.27 m above a 5 m-long horizontal channel, and we measured pore air pressure in the impact zone. During free fall, the granular mixtures accelerated and expanded to reach particle concentrations of 1.6–4.4 vol.% before they impacted the base of the channel. Upon impact, the particles accumulated to form concentrated granular flows with particle concentrations of 45–48 vol.% and pore air pressures that indicated almost full weight support for particle sizes ≤76 μm. Both the amount of pore pressure in the impact zone and the flow runout distance increased as we decreased the particle size and hence the hydraulic permeability of the concentrated granular mixtures. Our results suggest that pore gas pressure in concentrated pyroclastic density currents can be generated at the impact zone of collapsing fountains and that small particle size conferring low permeability and long pore pressure diffusion timescale is one of the main causes of long flow runout distances.

Plain Language Summary Collapse of volcanic eruptive fountains leads to the formation of pyroclastic density currents that can propagate over long distances. This mobility may be due to the high pore gas pressure in the pyroclastic mixture, which reduces intergranular friction. The origin of the pore gas pressure inside these mixtures is not well understood. We performed laboratory experiments to study the free fall from a hopper, and the subsequent impact on a rigid channel base, of dilute granular mixtures with particle concentrations of a few volume percent and different mean grain sizes. High-speed videos and pressure measurements showed that the granular mixtures compacted upon impact to form dense flows with high air pore pressure. As particle size decreased, both the pore pressure generated at the impact zone and the flow runout distance in the channel increased. For particle equal or smaller than 76 μm, the generated pore pressure was enough to counterbalance particle weight. Simple scaling arguments imply that full weight support would occur in nature for larger particle sizes. These results suggest that pyroclastic fountains can lead to the formation of concentrated ground-hugging currents with high interstitial pore gas pressure, and that particle size is key to controlling their travel distance.

Key Points:

- We present experiments on pyroclastic fountains by considering the impact of free-fall dilute granular mixtures on a horizontal channel base
- Accumulation of particles generates dense flows with pore gas pressure
- Pore gas pressure and flow runout distance increase as particle size decreases

Supporting Information:

Supporting Information may be found in the online version of this article.

Correspondence to:

B. Penlou,
Baptiste.PENLOU@uca.fr

Citation:

Penlou, B., Roche, O., & van den Wildenberg, S. (2023). Experimental study of the generation of pore gas pressure in pyroclastic density currents resulting from eruptive fountain collapse. *Journal of Geophysical Research: Solid Earth*, *128*, e2023JB027510. https://doi.org/10.1029/2023JB027510

Received 21 JUL 2023
Accepted 5 DEC 2023

Author Contributions:

Conceptualization: Olivier Roche, Siet van den Wildenberg
Data curation: Baptiste Penlou
Formal analysis: Baptiste Penlou, Olivier Roche, Siet van den Wildenberg
Funding acquisition: Olivier Roche, Siet van den Wildenberg
Investigation: Baptiste Penlou

1. Introduction

Pyroclastic fountain collapse during large-volume explosive volcanic eruptions generates ground hugging density currents (PDCs) that can travel distances up to ∼300 km and form widespread ignimbrites (Figure 1; e.g., Cas et al., 2011; Guzmán et al., 2020; Pacheco-Hoyos et al., 2018; Roche et al., 2022; Sparks et al., 1978). In the basal concentrated part of PDCs, sustained high interstitial pore gas pressure promoting low interparticle friction is a likely cause of the high mobility of these flows (Lube et al., 2019; Roche et al., 2016; Wilson, 1980). While seminal studies discussed possible internal and external sources of gas to cause fluidization of concentrated PDCs (Anderson & Flett, 1903; McTaggart, 1960; Wilson, 1980), recent advances have shown how pore gas pressure can arise in these mixtures from differential gas-particle motion (Breard et al., 2018; Chédeville & Roche, 2018; Lube et al., 2019), or from acoustic streaming (Valverde & Soria-Hoyo, 2015).

Methodology: Baptiste Penlou, Olivier Roche, Siet van den Wildenberg
Supervision: Olivier Roche, Siet van den Wildenberg
Validation: Baptiste Penlou
Visualization: Baptiste Penlou
Writing – original draft: Baptiste Penlou, Olivier Roche, Siet van den Wildenberg

In this study, we address the generation of pore gas pressure in concentrated PDCs that result from motion and compaction of a collapsing gas-particle mixture in the impact zone of a pyroclastic fountain. Though this hypothesis was discussed by Druitt and Sparks (1982) (their Figure 14), it was investigated quantitatively only recently through numerical simulations (Sweeney & Valentine, 2017; Valentine, 2020; Valentine & Sweeney, 2018). Here we investigate pyroclastic fountaining through laboratory experiments involving collapse of granular mixtures. This configuration was considered in earlier experimental studies, which focused on the dynamics of the analogue PDCs and did not address pore pressure generation mechanisms in the impact zone of a fountain (Breard & Lube, 2017; Dellino et al., 2007, 2010; Lube et al., 2015, 2019; Rowley et al., 2014), or were devoted to eruptions in water environment (Gilchrist et al., 2023). To the best of our knowledge, only one preliminary experimental work has presented general aspects of mixture compaction and associated pore pressure (Fries et al., 2021). In this context, the aim of our study is to investigate the mechanisms of granular mixture compaction and the possible generation of pore gas pressure in the impact zone of pyroclastic fountains. We consider in particular the effect of the particle size on the amount of pore gas pressure generated and on the runout distance of the flows that emerge from the impact zone. Finally, we discuss implications of our results for natural cases.

2. Methods

2.1. Experimental Device and Procedure

The experimental device consisted of a 60-L hopper whose aperture was at a height of 3.27 m above a ∼5 m-long horizontal channel (Figure 2). The hopper had a front wall and side walls inclined at 59° and 55°, respectively, and a vertical back wall (Figure 2b). All experiments were done with release from a rectangular aperture with a width of 10 cm, equal to that of the channel, and a length of 17 cm. Particles in the hopper were released by opening a trap door controlled by an electromagnet. Average mass fluxes from the hopper were ∼14−16 kg s^{-1}, with no systematic variation according to particle size. Below the hopper, a vertical open column bounded with rigid plastic sheets on each side prevented particle loss and guided the falling mixture into the channel. The latter consisted of six removable 1 m-long sections with smooth 10 cm wide aluminum base and 50 cm high Plexiglas side walls. The hopper was filled with 21 kg of silica glass beads of density ρ_p = 2,500 kg m^{-3}. We used six granular materials with a mean grain size varying from 29 to 269 μm (size distributions are given in Figure S1 in Supporting Information S1). We also considered the Sauter diameter, which accounts for the area of the particles and is relevant in case of gas-particle interactions (Breard et al., 2018). This diameter is defined as $d_{32} = 1/\sum_{i=0}^{N}(x_i/d_i)$, where x_i is the mass fraction in each size class and d_i the geometric mean diameter in this class. Note that the Sauter diameters are slightly smaller than the mean grain sizes because the materials are slightly polydisperse with a non-Gaussian size distribution (Table 1).

We used various types of sensors to investigate the processes at the impact zone in the channel. The pore gas (air) pressure was measured at a sampling rate of 50 Hz using a CSensors™ sensor (model 154N, precision of 6.9 Pa) placed at the back wall of the channel at a height of 4.55 cm above the channel base (Figure 2c). In order to prevent contact between the particles and the sensor membrane and to measure only the gas pressure, the sensor was placed in a casing inserted into the channel back wall and covered with a 36 μm mesh. We also measured the normal force imposed by the granular mixture on the channel base using a piezoelectric sensor (Kistler™ 9317B). The upper part of the sensor was screwed on a 6 × 6 cm flush fitting aluminum plate inserted into the base of the channel at a distance of 14 cm from the backwall while its lower part was connected to a rigid structure fixed to the base of the channel (Figure 2d). A gap of 150 μm between the margins of the plate and the channel base allowed the plate and the top of the sensor to move freely upon impact of the falling mixture. A very thin plastic film fixed with tape on the channel base covered the plate to prevent particles falling into the gap and block the movement of the plate.

All the experiments were filmed with a Photron Fastcam SA3 high speed video camera at a rate of 250 frames per second to document the accumulation of the particles in the channel and the emergence of granular flows. A LED panel was placed behind the transparent wall opposite the camera in order to improve the contrast between the particles and the background. The videos were analyzed with ImageJ* (Schneider et al., 2012) to produce kymographs along a vertical line at the center of the falling leading head regions and the impact zone. For each kymograph, the interfaces between the falling mixture or the granular bed and the background were determined using home written Matlab routines based on thresholds of pixel intensity. Next, the impact velocity of the falling leading head and the height of the accumulated granular material were calculated. We used a toggle switch to synchronize all measurements (i.e., video, pressure and force) with the opening of the hopper trap door. When the

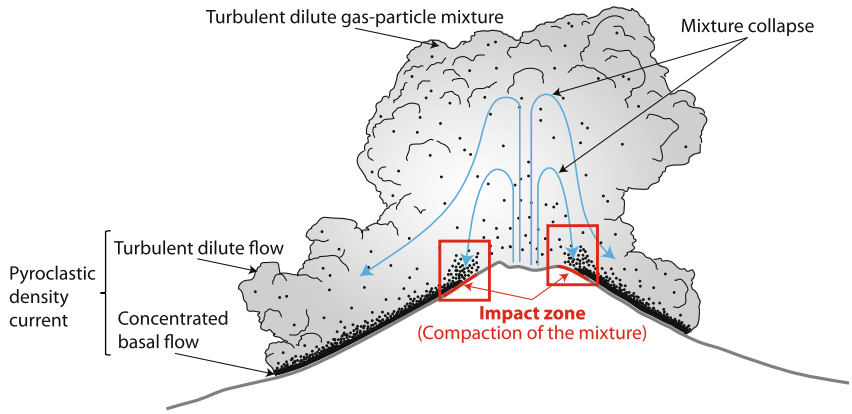

Figure 1. Sketch of a pyroclastic fountain. A gas-particle mixture emitted from the vent experiences gravitational collapse. Pyroclastic density currents emerge from impact zones and consist of a concentrated basal part topped by a dilute suspension. The gas phase corresponds to gray shades and particles are represented by black dots.

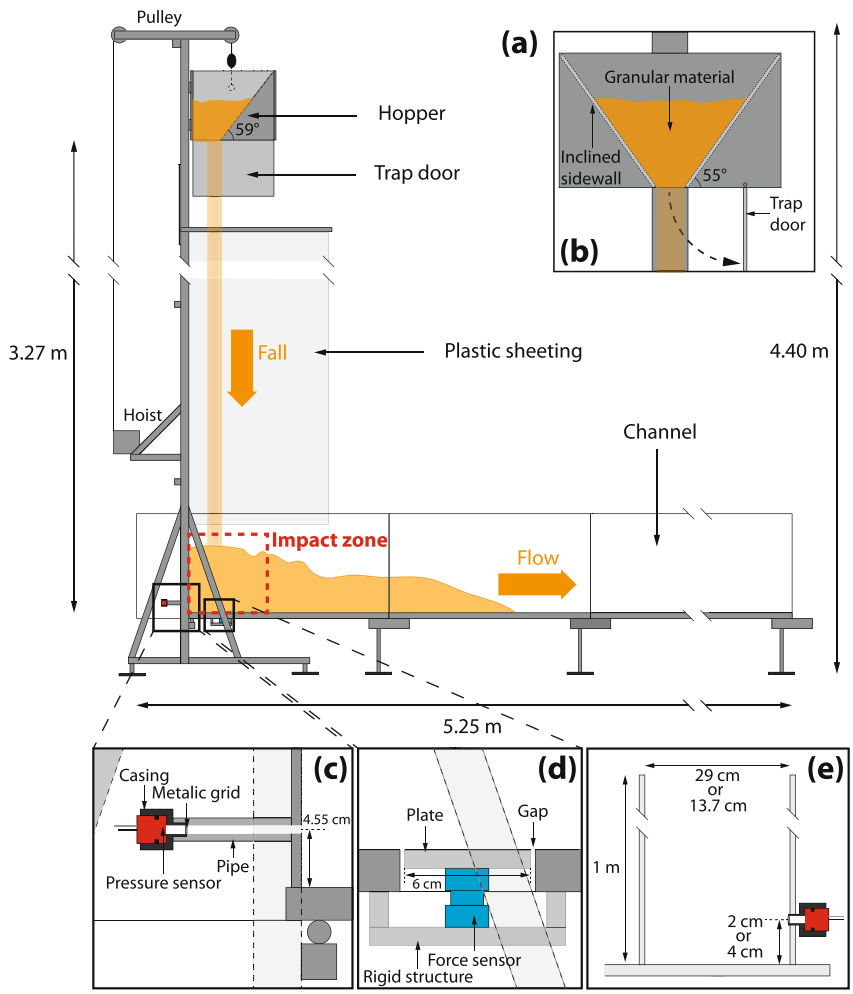

Figure 2. (a) Sketch of the experimental device. (b) Cross section longitudinal view of the interior of the hopper with the inclined sidewalls. (c) Cross section of the air pressure measurement device with the sensor at the backwall of the channel. (d) Cross section of the force measurement device. (e) Complementary cylindrical devices with a pressure sensor and placed at the impact zone to determine the concentrations of the free-fall mixtures and of the granular beds.

Table 1
Physical Parameters in Nature and Experiments

Symbol	Unit	Pyroclastic fountains	Experiments	Parameter
d_p	m	$10^{-5} - 10^{-1}$	$29 - 269 \times 10^{-6}$	Mean particle diameter
d_{32}	m	–	$27 - 221 \times 10^{-6}$	Particle Sauter diameter
c_a	m s^{-1}	~330	~330	Sound speed in air
μ_a	Pa s	$\sim 10^{-5}$	1.8×10^{-5}	Air dynamic viscosity
ρ_a	kg m^{-3}	~1	1.2	Air density
ρ_p	kg m^{-3}	700–2,500	2,500	Particle density
Collapse phase				
ϕ_1	–	$10^{-3} - 10^{-2}$	$1.6 - 4.35 \times 10^{-2}$	Particle volume fraction
μ_1	Pa s	$\sim 10^{-5}$	$1.92 - 2.15 \times 10^{-5}$	Mixture dynamic viscosity
ρ_1	kg m^{-3}	$10^0 - 10^2$	41 – 110	Mixture density
U_p	m s^{-1}	$10^{-4} - 10^1$	$10^{-1} - 10^0$	Particle settling velocity
U_1	m s^{-1}	40 – 500	6.74 – 8.17	Mixture fall velocity
R	m	$10^2 - 10^3$	10^{-1}	Impact zone width
H	m	$10^2 - 10^4$	3.27	Collapse height
Flow phase				
ϕ_2	–	0.3 – 0.6	0.4 – 0.55	Particle volume fraction
ρ_2	kg m^{-3}	210 – 1,500	1,000 – 1,376	Mixture density
D	m^2 s^{-1}	$10^{-4} - 10^1$	$10^{-3} - 10^{-2}$	Diffusion coefficient
k_2	m^2	$10^{-13} - 10^{-4}$	$10^{-12} - 10^{-10}$	Hydraulic permeability
U_2	m s^{-1}	$10^1 - 10^2$	2.42 – 3.9	Flow front velocity
h	m	$10^0 - 10^1$	0.11 – 0.13	Flow thickness
L	m	$10^3 - 10^5$	1.13 – 4.57	Flow runout distance
γ	s^{-1}	$10^1 - 10^2$	22 – 30	Flow shear rate

Note. Typical values are from Sparks et al. (1978), Burgisser et al. (2005), Valentine and Sweeney (2018), Breard et al. (2018), and Fries et al. (2021).

switch was turned off, a 3 mV trigger was sent to both the pressure and force measurement acquisition systems while the LED light was turned on (cf. video recording) and the electromagnet was turned off to release the trap door. We conducted 22 experiments with at least 3 experiments per particle size to check for reproducibility of the results. The duration of an experiment was about 1.5–2.5 s from opening of the trap door to final deposition of particles in the channel. Deposits thickness was measured every 20 cm from the back door of the channel using a ruler. The typical variability in runout distance was about 3 cm except for the smallest particles for which the front deposit was poorly defined as it was a diffuse spread not forming a coherent deposit, and we estimated an error of about 50 cm.

2.2. Measurement of Particle Volume Fraction

We did complementary experiments to estimate, from air pressure measurements, the particle volume fraction in the mixtures in free fall just before impact (ϕ_1) and in the granular flows formed upon impact (ϕ_2). We used the same mass of material and fall height as in experiments with the channel. For these complementary experiments, we investigated the collapse of granular mixtures in cylindrical containers to overcome significant lateral movement of the air and of the granular material inherent in the channel configuration. Measurements were conducted in 1-m high Plexiglass cylinders glued on horizontal plates positioned at the height of the channel base in the impact zone (Figure 2e). We investigated the particle volume fraction in the falling mixtures by using a cylinder with an inner diameter of 13.7 cm, which was slightly larger than the typical width of the granular column collapsing from the hopper. In order to investigate accurate measurements of the temporal variation in pressure

just before the impact of the materials, we used the same sensors as in the channel experiment and a fast acquisition system with a sampling frequency of 1,000 Hz. As shown in Figure 2e, the pressure sensor was placed for these experiments on the side of the cylinder at a height of 4 cm from the base. In this configuration, lateral air escape was negligible and we could infer the particle volume fraction assuming that interstitial air was moving with particles at the same speed from

$$P_d = \frac{1}{2}\left[\rho_p\phi_1 + \rho_a(1-\phi_1)\right]U_1^2 \quad (1)$$

where P_d is the dynamic pressure, ρ_p and ρ_a are the density of the particles and the air, respectively, ϕ_1 is the particle concentration of the mixture, and U_1 the front velocity of the mixture just before impact and determined from high speed videos. Since $\rho_a \ll \rho_p$, we assumed

$$P_d \sim \frac{1}{2}\rho_p\phi_1 U_1^2 \quad (2)$$

Upon impact, the granular mixture compacted rapidly, to form a dense bed due to energy dissipation by interparticle collision. We attempted to investigate particle volume fractions in flows formed in the channel but chaotic motion of the material and rapid variation of the height of material prevented reliable estimates. For this reason, we used a 29-cm diameter cylinder in the impact zone. This reduced the magnitudes of temporal variations in flow height and allowed to constrain time-series of flow height more confidently. A pressure sensor was placed 2 cm from the base of the cylinder (Figure 2e). We estimated the particle volume fraction in the flow (ϕ_2) from

$$P_l = \left[\rho_p\phi_2 + \rho_a(1-\phi_2)\right]gh_c \quad (3)$$

where P_l is the pore air pressure, g is the gravitational acceleration, and h_c is the height of the granular material in the cylinder. As the weight of the air is negligible compared to that of the particles, and assuming a negligeable pore fluid pressure diffusion during the compaction, Equation 3 simplifies as

$$P_l \sim \rho_p\phi_2 gh_c \quad (4)$$

All of these additional experiments were recorded at 250 frames per second, and the videos were analyzed to calculate both the impact velocity of the mixtures in the small cylinder and the height of granular material in the large cylinder. In total, 10 experiments were conducted, consisting of 2 experiments for each particle size (small and large cylinder).

3. Scaling Analysis

We present a scaling analysis to estimate the degree of dynamic similarity between our experiments and the natural system. Table 1 gives the physical parameters of the gas and solid phases. Note that some of the parameters used to define the dimensionless numbers (Table 2) are deduced from others, such as the density ($\rho_j = \rho_p\phi_j + \rho_f(1-\phi_j)$) or the viscosity ($\mu_j = \mu_a\left(1-(\phi_j/\phi_{\max})^{-2.5}\right)$, with $\phi_{\max} = 0.64$) of falling dilute ($j = 1$) or flowing concentrated ($j = 2$) mixtures, the reduced gravity $g' = ((\rho_1 - \rho_a)/\rho_1)g$, and the average flow shear rate ($\gamma = U_2/h$). We determined the terminal settling velocity of particles using the method of Rhodes (2008). Since the particle concentration varied considerably during the experiments we present in Table 2 two groups of dimensionless numbers that describe the physics of the dilute (collapse phase) and the concentrated (flow phase) mixtures (Table 2).

In general, the ranges of values of the dimensionless numbers in experiments overlap those of the natural cases and are significantly smaller, essentially because the granular mixtures in experiments are significantly less polydisperse than in nature. This means that our analogue configuration captures only a subset of the gas-particle feedback mechanisms expected to occur in natural pyroclastic fountaining. For dilute mixtures during the collapse phase, we highlight that the Stokes and Stability numbers in experiments indicate moderate to poor air-particle coupling and thus tendency for particle accumulation in the impact zone, which is a fundamental aspect of our study. The Reynolds number in our experiments is smaller than in nature but it indicates fully turbulent flow ($\mathrm{Re} > 10^3$) and shows that the experiments are dynamically similar to natural dilute volcanic mixtures (Andrews & Manga, 2012). The Mach number shows an important limitation of the experiments, which are in the subsonic regime whereas supersonic conditions and related compressible flow phenomena such as shocks, high pressure

Table 2
Dimensionless Number in Nature and Experiments

Number	Definition	Pyroclastic fountains	Experiments	Description
Collapse phase				
Mach	$Ma = \frac{U_1}{c_1}$	$10^{-1} - 10$	$0.14 - 0.21$	Ratio of falling mixture speed over mixture sound speed. Subsonic case ($Ma < 1$)
Reynolds	$\mathrm{Re} = \frac{RU_1\rho_1}{\mu_1}$	$10^{9} - 10^{12}$	$1.56 \times 10^{6} - 2.94 \times 10^{6}$	Ratio of inertial forces over viscous forces. Turbulent flow ($\mathrm{Re} > 10^3$)
Richardson	$Ri = \frac{Hg'}{U_1^2}$	$10^{-1} - 10^{1}$	$0.47 - 0.69$	Ratio of potential energy over kinetic energy. Transitional regime ($Ri \sim 1$)
Stability	$\Sigma = \frac{(\rho_p - \rho_a)d_p^2 g}{18\mu_1 U_1}$	$10^{-8} - 10^{2}$	$10^{-1} - 10^{1}$	Ratio of gravity (buoyancy) force of a particle over viscous drag. Moderate to poor gas-particle coupling in experiments ($\Sigma \geq 0.1$)
Stokes	$St = \frac{(\rho_p - \rho_a)d_p^2 U_1}{18\mu_1 R}$	$10^{-5} - 10^{6}$	$10^{-1} - 10^{1}$	Particle response time over timescale of the flow. Moderate to poor gas-particle coupling in experiments ($St \geq 0.1$)
Flow phase				
Bagnold	$Ba = \frac{\rho_p \gamma d_p^2 \phi_2}{\mu_a(1-\phi_2)}$	$10^{-3} - 10^{8}$	$10^{0} - 10^{2}$	Ratio of particle collisions over viscous fluid stresses (early stages). Viscous to transitional regime ($40 < Ba < 450$)
Darcy	$Da = \frac{\mu_a}{\rho_p \gamma k_2 \phi_2}$	$10^{-7} - 10^{4}$	$10^{0} - 10^{2}$	Viscous fluid-particle stresses over particle inertial stresses (early stages). Pore fluid pressure buffers particle interactions in experiments ($Da \geq 1$)
Inertial	$I = \gamma\sqrt{\frac{\rho_p d_p^2}{p}}$	$10^{-6} - 10^{-1}$	$10^{-3} - 10^{-2}$	Ratio of particle collisions to particle friction (late stage). Friction controls flow dynamics ($I < 0.3$)
Pressure	$\mathrm{Pr} = \frac{D\sqrt{L/g}}{h^2}$	$10^{-4} - 10^{3}$	$10^{-2} - 10^{0}$	Ratio of flow timescale (cf. pressure advection) over pressure diffusion timescale ($\mathrm{Pr} \leq 1$)

Note. Typical values are from Iverson and Denlinger (2001), Valentine and Sweeney (2018), Lube et al. (2015) and Fries et al. (2021).

gradients and subsequent decompression effects can occur in nature (Valentine & Sweeney, 2018). Note that in Table 2, c_1 is the mixture sound speed defined as $c_1 = c_a\sqrt{\rho_a/\rho_p}(\phi_1(1-\phi_1))^{-1/2}$ with $c_a = 330$ m s^{-1} (see Valentine & Sweeney, 2018). For concentrated mixtures during the flow phase in experiments, the Bagnold and Darcy numbers indicate that fluid stresses dominate interparticle stresses and that pore fluid pressure can be high at early stages of propagation, while the pressure number indicates relatively slow pore pressure diffusion during flow emplacement. At late stages when pore pressure has diffused, the inertial number indicates a frictional regime (note that p in Table 2 is the solid pressure).

4. Results

The results are structured as follows. First, we present the general observations made during the experiments. Second, we delve into the characteristics of the collapsing mixtures, such as impact velocities and concentrations measured in complementary experiments. Finally, we investigate the properties of the dense beds formed upon impact, including pore pressure and degree of fluidization, flow runout distance and morphology of the deposits. Preliminary findings regarding the forces generated in the impact zone are presented as Supporting Information S1.

4.1. General Observations

A granular mixture released from the hopper is in free fall and therefore accelerates continuously and expands until it enters into the channel (Figure S2 in Supporting Information S1). The falling material is a granular column with an almost constant width of ~8–10 cm, smaller than the hopper aperture, and with a leading head region

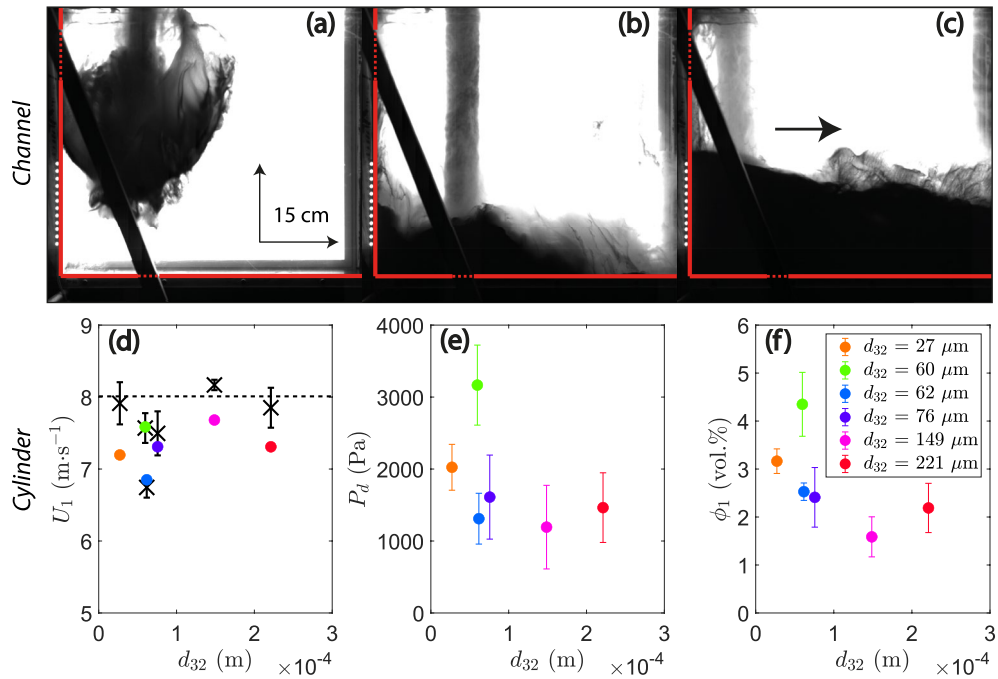

Figure 3. Particle fall and accumulation in the impact zone of the channel (d_{32} = 62 μm). (a) The granular leading head region before impact. Variations in darkness are attributed to variable thickness of granular material across the channel and different amounts of light transmitted through. (b) Steadily falling column, and formation of a dense granular bed. (c) Flow propagation in the channel. (d) Fall velocity of the granular mixtures before impact as a function of the particle size in the channel (black crosses) and in the 13.7-cm diameter cylinder (colored dots) configurations. Error bars on crosses represent the standard deviations over all experiments. The theoretical free fall velocity is shown by the black dotted line. (e) Dynamic pressure measured in the 13.7-cm diameter cylinder. (f) Particle concentration of the falling mixtures before impact, calculated from Equation 2 using the measurements in the cylinder configuration in (d) and (e) (see Section 2). Error bars in (e) and (f) represent fluctuations in the pressure and concentration values over the black or red portions of signals shown in Figure S3 in Supporting Information S1, which correspond to time intervals between the last maximum value of ϕ_1 and the time of impact.

larger than the collapsing column and which widens over time (until ~18–26 cm wide before impact) probably due to drag caused by the ambient air (Figure 3a). Initially, the granular column does not fall along the backwall of the channel although the latter is vertically aligned with that of the hopper, which suggests a possible influence of the geometry of the hopper on the particles release mechanism (Figure 3b). Then the column progressively approaches the channel backwall and finally tangents it (Figure 3c). The free-fall mixtures are visually homogeneous, except for the experiments with Sauter mean diameters of 27 μm that formed particle aggregates. Note that we dried this finely-grained material to eliminate ambient moisture and in this regard the aggregates could result from electrostatic forces or the release mechanism from the hopper.

Upon impact with the base of the channel, the particles accumulate to form a concentrated mixture, which then propagates in the channel as a dense gas-particle flow. Different types of flow are observed depending on the size of the particles. With 27, 60, 62, and 76 μm diameter particles, a concentrated basal flow is topped by a dilute turbulent suspension (see Movies S1 and S2). For increasing particle size, the thickness of the dilute layer decreases and for particle sizes larger than 76 μm only a concentrated flow is observed.

4.2. Impact Dynamics

4.2.1. Velocities and Particle Concentrations of the Falling Mixtures

We first estimate the front velocities of the falling mixtures just before the impact on the channel base. For each case, we measure the position of the leading head region of the falling mixture during its descent into the channel, along a vertical line at the center of the head (Figure S2 in Supporting Information S1). The front velocity of the head is nearly constant over this short distance and we assume a linear relationship between the front

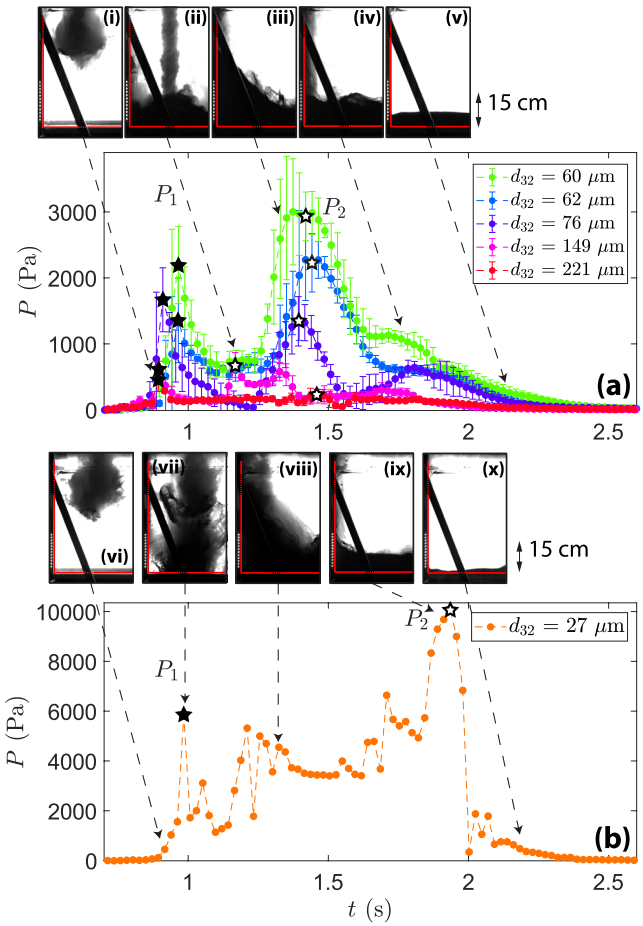

Figure 4. Pore air pressure measured in the impact zone and corresponding snapshots as a function of time for particle sizes $d_{32} > 27$ μm in (a). The error bars represent standard deviations for four experiments and indicate good reproducibility. (i)–(v) are snapshots from an experiment with particles of $d_{32} = 62$ μm and corresponding to times indicated by the dashed arrows in (a). (b) Data for one of the four experiments with $d_{32} = 27$ μm and (vi)–(x) are snapshots of this experiment. Red lines in the snapshots indicate the base and the back wall of the channel, and time zero corresponds to opening of the hopper trapdoor. Maximum pressure values P1 and P2 discussed in the main text are shown by stars in (a) and (b).

position and time to obtain the fall velocities of the mixtures upon impact. Figure 3d shows that these velocities are slightly lower than the theoretical free fall velocity $U_t = \sqrt{2Hg}$, ($\geq 0.93U_t$) which demonstrates some drag of the ambient air. For most mixtures, the fall velocities in the cylinder are lower than those in the channel, suggesting possible higher drag as the air could not escape laterally. The fall velocity of the mixture of 62 μm diameter particles is $\sim 0.85U_t$, which suggests a higher drag than for other mixtures. Note that all these fall velocities are well above the terminal settling velocities of individual particles $\sim 10^{-1}$–10^{0} m s^{-1} (see Table 1). We then use the fall velocities and the pressure signals (Figures 3d and 3e) in the cylinder configuration to calculate the particle concentrations of the falling mixtures (ϕ_1) from Equation 2. Figure 3f shows ϕ_1 determined from time intervals ~0.02–0.10 s just before impact (see Figure S3 in Supporting Information S1). The concentrations vary between ~1.6 to 4.4 vol.%, indicating that the granular mixtures are dilute before impact, in agreement with the findings of Fries et al. (2021), and we find no correlation between ϕ_1 and the particle size. Note that the leading head seems more concentrated than the material behind since it is darker on video images (Figures 3a and 3b). However, this is probably due to the greater width of the head and as less light is transmitted through.

4.2.2. Pore Air Pressure in the Dense Flows

Next we investigate pore air pressure in the granular flows formed at the impact zone (Figure 4). For each d_{32}, the experiments were repeated 4 times and the pressure signals showed good reproducibility except for the 27 μm diameter particles, as discussed below. To appreciate the processes in the impact zone it is important to keep in mind that pore pressure could depend on the motion of the mixture, the air-particle drag, and the thickness of the granular material above the sensor.

Overall, we find for particles larger than 27 μm an initial pressure peak upon impact (duration ~0.11–0.28 s), P_1, followed by a longer phase of overpressure as the granular flow emerges (duration ~0.81–1.12 s), P_2 (Figure 4a). After impact and spreading of the head of the falling granular column, the pressure increases rapidly as the column migrates toward the sensor at the channel backwall and the thickness of the material above the sensor increases rapidly (Figure 4a(ii)–(iii)). Finally, the pressure drops relatively slowly as the particle supply stops and the granular bed height decreases due to the outflow of the granular flow down the channel (Figure 4a(iv)). Instead, the pressure signals for the 27 μm diameter particles are not reproducible and we show the results for one experiment (Figure 4b). In this case, particles are released from the hopper more evenly over time than for larger particles, possibly because of cohesion effects that cause the formation of aggregates. Compared to larger grain sizes after impact, the pressure increases at a lower rate as aggregates impact the channel base in the form of successive pulses, which create a discontinuous accumulation of particles over time and could cause transient pressure variations. The aggregates are a likely cause of the non-reproducibility of the pressure signals. Note that though the signals are not reproducible the maximum pressure values P_1 and P_2 show variations of only ~10%. A relatively rapid drop in pressure occurs as soon as particle fall ceases and the height of the granular bed decreases when the material spreads in the channel. A notable outcome of these measurements is that the maximum pore pressure increases as the particle size decreases. We discuss this point in more detail below.

We estimated the particle concentrations in the dense granular flows from pore air pressure measurements in the cylinder configuration and the height of the granular bed h_c in the cylinder using the method described in Section 2.2 (Figure 5). A short pressure peak upon impact is followed by a second longer phase of overpressure as the granular beds build up from compaction; note that the second phase in both configurations begins at $t \sim 1.2$ s but it lasts longer and has a lower decay rate in the cylinder configuration because the material is not evacuated

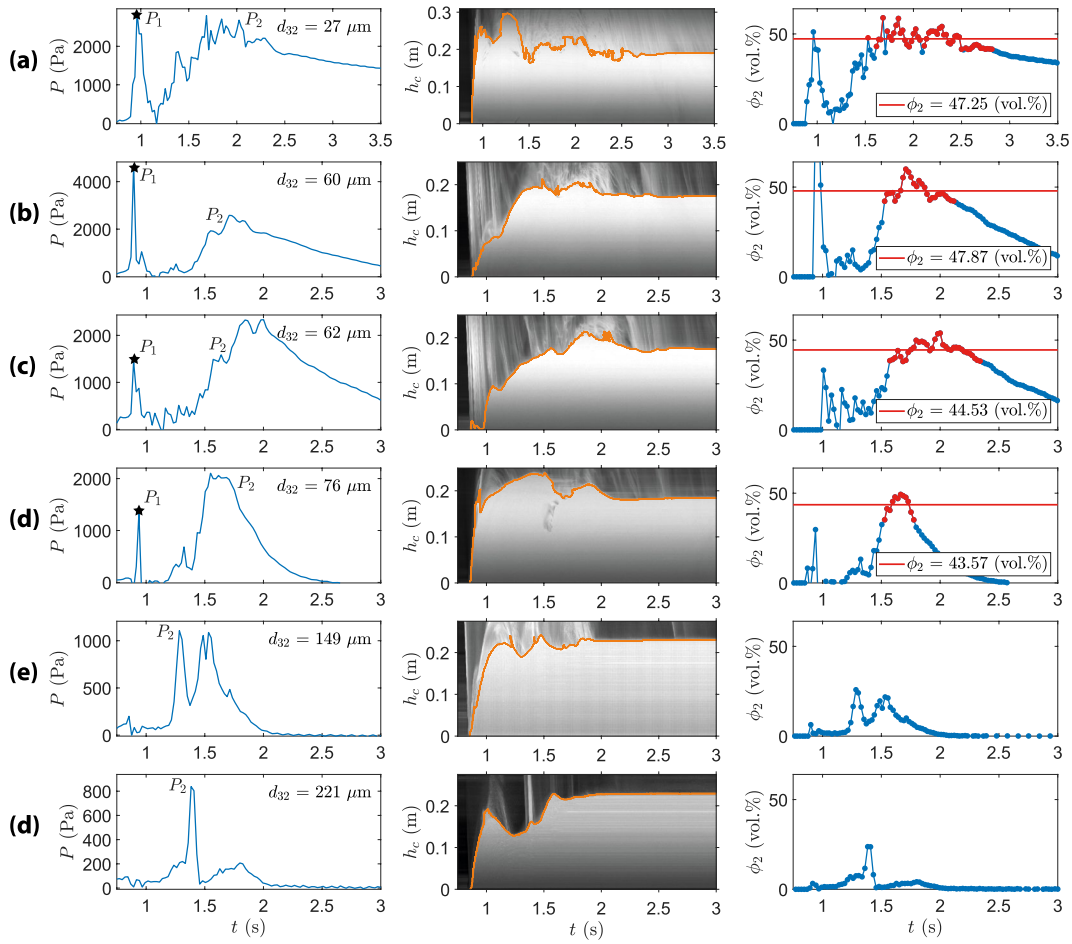

Figure 5. Measurements in the 29-cm diameter cylinder at the impact zone as function of time for (a) $d_{32} = 27$ μm, (b) $d_{32} = 62$ μm, (c) $d_{32} = 60$ μm, (d) $d_{32} = 76$ μm, and (e) $d_{32} = 149$ μm and (f) $d_{32} = 221$ μm. Time t_0 corresponds to the opening of the hopper trapdoor. (left column) Pore fluid pressure. Maximum pressure values P_1 and P_2 are shown. (center column) Kymographs presenting the pixel intensity in time along a vertical line at the center of the cylinder, from which the height of the granular bed is determined (orange lines). Note that orange lines may curl backward but there is only one corresponding bed height at the times at which pressure data used to calculate particle concentrations are available. (right column) Particle concentrations calculated with Equation 4 from the pore pressure in the left column and the bed height in the center column. Red dots indicate particle concentrations greater than 70% of the maximum value and are used to determine average flow concentrations given by red lines.

laterally as in the channel. This similarity between the pressure signals measured in the two configurations suggests that particle concentration in the channel can be inferred from data acquired in the cylinder. For each movie, we used ImageJ* to produce a kymograph along a vertical line at the center of the cylinder. The height of the bed h_c over time was then determined using a pixel threshold value ranging from less than 0.3 to 0.8 of the maximum intensity in the kymographs (Figure 5, second column). The data of pore pressure and flow height permitted us to estimate the particle concentration from Equation 4, assuming a negligible dynamic component. Note that the particle concentrations determined this way are minimum estimates. The maximum pore pressure measured upon impact and then as particles accumulate varies generally inversely with the particle size and it decreases significantly at $d_{32} \geq 149$ μm (Figures 5e and 5f). The bed height grows at different rates to reach a constant value of ~20 cm. The corresponding maximum particle concentrations for $d_{32} \leq 76$ μm are ~45–48 vol.%, which show that the granular beds are close to their maximum packing ~58 vol.%. Small pore pressure, probably due to weak air-particle coupling, for $d_{32} \geq 149$ μm does not allow reliable estimates of particles concentrations and in the following we will assume that the concentrations of these mixtures are identical to that for smaller particles.

Assuming that our estimates of particle concentrations in the cylinder are also representative of the channel configuration we use them to determine the amount of pore pressure in the granular flows in the impact zone

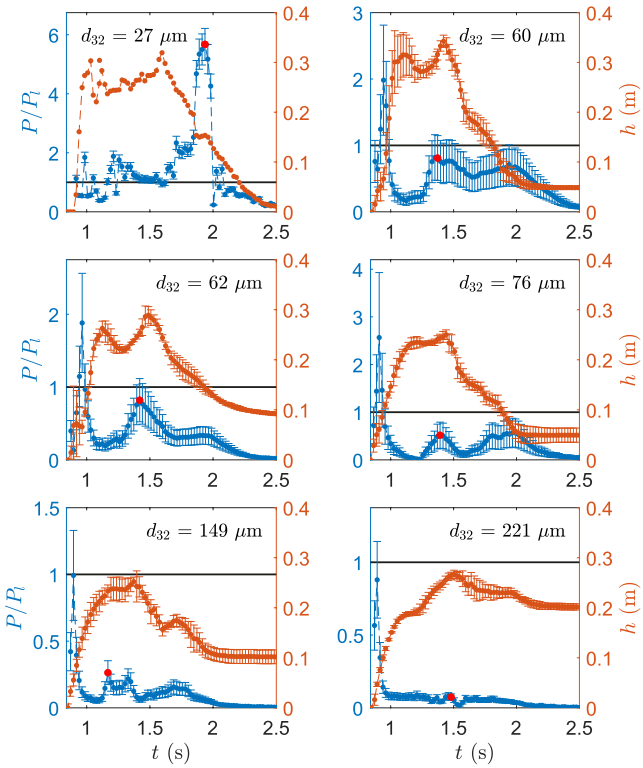

Figure 6. Ratio P/P_l for the granular flows at the impact zone in the channel configuration and the corresponding flow heights (h) as a function of time for different particle sizes. The horizontal black lines indicate $P/P_l = 1$. Note that the red points correspond to maximum P_2/P_l. Error bars for h correspond to the standard deviation over the experiments and the error bars for P/P_l are calculated via standard error propagation, with errors in P and h due to experimental variability and errors in ϕ_2 from temporal fluctuations (indicated by red symbols in Figure 5, except for the smallest particles for which h is not reproducible). For d_{32} = 149 and 221 μm we assume particle concentrations of 45 vol.% to calculate P/P_l.

of the channel (Figure 6). To do this, we calculate the ratio of the pore air pressure measured in the channel, P, to the theoretical lithostatic pressure, $P_l \sim \rho_p \phi_2 g h$, with h the flow thickness at the channel backwall and ϕ_2 the particle concentration given in Figure 5. Note that since ϕ_2 is determined at times intervals corresponding to the second pressure peak P_2, then P/P_l at other time intervals must be considered with care. For $d_{32} \leq 76$ μm, P/P_l first increases sharply for a short time upon impact of the granular material. Then P/P_l drops rapidly before increasing again during the growth of the granular flow (i.e., increase of h), and high P/P_l values are observed over durations that correlate negatively with the particle size. During this second peak the maximum values, P_2/P_l, are close to 1 for $d_{32} \leq 60$ μm (see Figure 7a) and therefore indicate nearly full bed weight support, which is also supported by the presence of surface waves and air bubbles. For larger grain sizes, P_2/P_l indicates moderate ($d_{32} = 76$ μm) to negligible ($d_{32} = 149$ and 221 μm) weight support. At late stages, P/P_l decreases irregularly and finally becomes zero. A notable exception is for $d_{32} = 27$ μm for which P/P_l increases first sharply while the flow height decreases, possibly because of late aggregates impacting the bed and causing significant pressure.

We further investigate the process of particle accumulation in the impact zone at the time the maximum pore pressure P_2 is measured. The ratio P_2/P_l (see Figure 6) decreases with increasing particle size and is negligible for particle sizes larger than ~100 μm (Figure 7a). We estimate the relative velocity between the air and the particles $(\bar{U})$ from the Darcy equation, assuming that the inertial forces are negligible, so that

$$\bar{U} = \frac{P_2 k_2}{h_2 \mu_a} \tag{5}$$

where k_2 and h_2 are the bed permeability and bed height at P_2, respectively. The permeability is estimated according to

$$k_2 = \frac{(1-\phi_2)^3 d_{32}^2}{150 \phi_2^2} \tag{6}$$

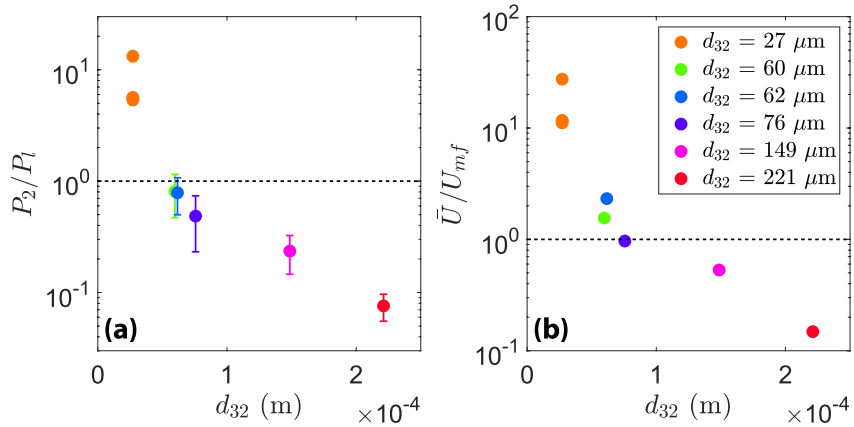

Figure 7. (a) Ratio P_2/P_l as a function of the Sauter diameter. The dashed line indicates $P_2/P_l = 1$. Error bars are calculated via standard error propagation, with errors in P_2 and h_2 from the standard deviation over the experiments and errors in ϕ_2 are from the fluctuations along the red portions in Figure 5. (b) Ratio of the relative air-particle velocity during mixture compaction, $\bar{U}$, and the minimum fluidization velocity, U_{mf}, estimated from $k_2' g\left(\rho_p \phi_2' + \rho_a\left(1-\phi_2'\right)\right)/\mu_a$, with k_2' the reference permeability estimated using the maximum concentration of the granular mixtures $\phi_2' \sim 0.58$ at random packing. The dashed line indicates $\bar{U}/U_{mf} = 1$

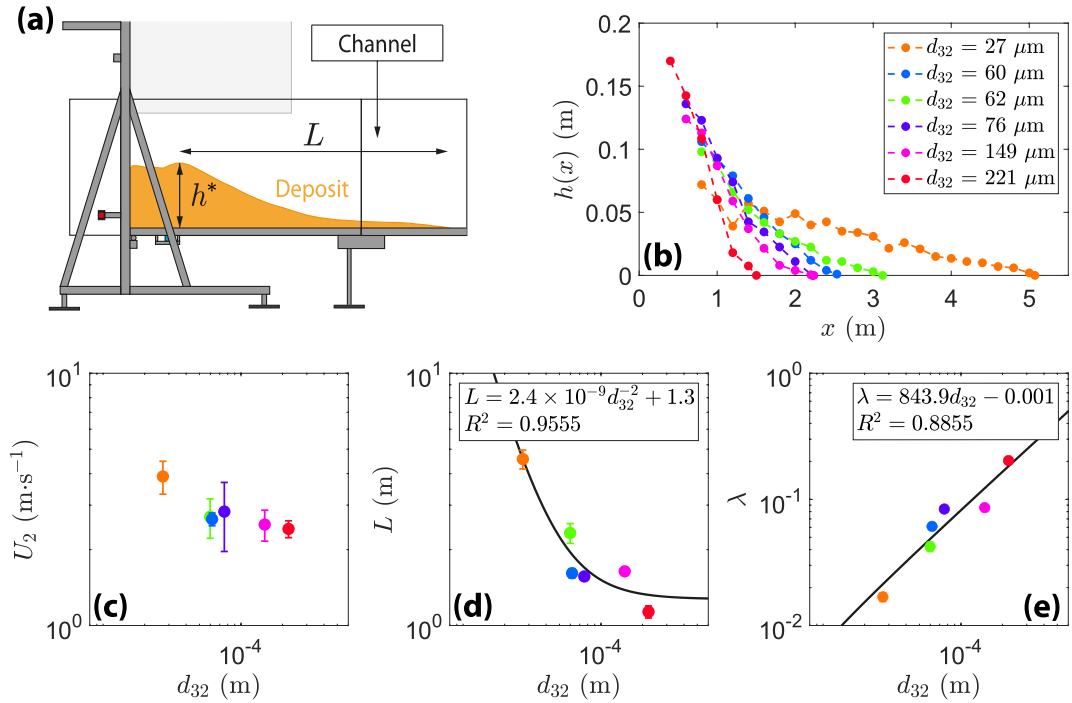

Figure 8. Characteristics of the granular flow deposits. (a) Sketch of a deposit with maximum deposit height (h^*) and runout distance (L). (b) Deposit thickness as function of distance. (c) Flow front velocity and (d) Runout distance as a function of the Sauter diameter. In panel (d), the offset 1.3 in the fit corresponds to the minimum runout distance related to the fall height, mass and material properties of particles used. (e) Aspect ratio ($\lambda = h^*/L$) of the deposits as a function of the Sauter diameter. Error bars in panels (c), (d), and (e) represent the standard deviations over all experiments.

where ϕ_2 is the particle concentration given in Figure 5 for $d_{32} \leq 149$ μm and assumed equal to 45 vol.% for $d_{32} > 149$ μm. The velocities $\bar{U}$ are of the order of 10^{-2} m s^{-1} and are larger than or equal to the minimum fluidization velocities (U_{mf}) for $d_{32} \leq 76$ μm or smaller than U_{mf} for larger grain sizes. These velocities give particle Reynolds numbers less than ~0.1, which suggest that our assumption of negligible air inertial effects is reasonable. These results confirm that upon impact mixtures of particles with $d_{32} \leq 76$ μm and mixtures of coarser particles have full and partial bed weight support, respectively.

4.3. Granular Flows and Associated Deposits

Finally we discuss the characteristics of the granular flows generated in the impact zone and of their deposits in the channel as function of the particle size (Figure 8). The flow front velocity (U_2) estimated from kymographs (Figure S5 in Supporting Information S1) shows a weak negative correlation with the particle size (Figure 8c). A similar tendancy is observed for the flow runout distance but the latter increases notably for particle sizes smaller than ~100 μm. Considering that the runout distance scales with $U_2 \times t_2$, with t_2 the flow timescale, and assuming that this timescale is similar to the pore pressure diffusion timescale t_d, proportional to h^2/D with $D \propto k/((1-\phi_2)\mu_a\beta)$ and β the air compressibility, then the runout distance is expected to vary inversely with $1/d_{32}^2$ according to Equation 6 and as the other parameters vary little. The data in Figure 8d support the idea that the runout distance depends essentially on the particle size. This dependence translates into more elongated deposits with decreasing thickness in the impact zone as the particle size decreases. Therefore, the corresponding aspect (thickness-to-length) ratio of the deposits correlates positively with the particle size (Figure 8e).

5. Discussion

5.1. Mechanisms in Experiments

The main outcome of our experiments is that the compaction of falling mixtures with particle concentrations of ~1.6–4.4 vol.% in the impact zone generates concentrated flows with varying amount of pore pressure depending

on the particle size. The high Stokes number of the particles (10^{-1}–10^{1}), as defined for our study, can explain the efficient decoupling between the particles and the interstitial air, which has two consequences: a high relative velocity between the descending particles and the ascending air, and an accumulation of the particles at particle volume concentrations close to that of maximum packing value. The particle size is essential in this configuration because it controls both the permeability of the granular flow and the weight of the particles counterbalanced by the drag force exerted by the air. Therefore, pore air pressure can be generated as the granular flow builds up (Breard et al., 2018; Chédeville & Roche, 2018) and the amount of pressure correlates negatively with the particle size. In our experiments, almost full bed weight support is achieved at $d_{32} \leq 76$ μm. The increase in the amount of pore pressure in the impact zone as the particle size decreases translates to increased flow runout distance and horizontal elongation of the deposits. In principle, the flow dynamics depend both on the amount of pore fluid pressure generated upon impact and on the ratio of the timescale of pressure advection to the timescale of pressure diffusion (Iverson & Denlinger, 2001, see pressure number in see Table 2). Flows of fine particles, for which the generated pore fluid pressure remains high for an extended period due to slow diffusion during propagation in the channel (see Figures 4–7), have longer runout distances compared to flows of coarser particles. Our results show that, at laboratory scale, flow runout varies significantly for particle sizes smaller than $d_{32} \sim 100$ μm, corresponding to permeabilities $k_2 \sim 10^{-10}$ m^2 from Equation 6. In summary, the smaller the particle size (and flow permeability), the greater the pore pressure in the impact zone, the longer the pressure diffusion during flow emplacement, and the longer the flow runout distance.

5.2. Implication for Natural Cases

Before we discuss implications of our results for natural systems it is important to keep in mind that the experiments have several limitations and apply essentially to subsonic cases ($Ma < 1$) with large amount of particles with large Stokes numbers. In nature, most mixtures with high impact speeds (50–150 m s^{-1}) and concentrations (∼0.1) are supersonic ($Ma > 1$). Under these conditions, the mixtures decelerate as they approach the impact area and steep pressure gradients and shocks are created (Sweeney & Valentine, 2017). Our study suggests that the accumulation of particles with relatively high Stokes numbers and the emergence of concentrated PDCs with high pore gas pressure can occur readily in the impact zone of pyroclastic fountains, in agreement with findings from numerical simulations (Valentine & Sweeney, 2018, their Figure 9b). The high pore gas pressure is then advected outside the impact area as the concentrated current propagates away (Valentine, 2020, their Figure 5). In general, the mechanisms that operate in experiments with particles of mean sizes close to those of most pyroclastic mixtures should be enhanced at larger length scales in nature. All else being equal, higher impact velocities (up to the terminal mixture velocity) due to greater fall heights will allow the generation of high pore pressure in coarser mixtures, while greater flow thicknesses will result in relatively slower pore pressure diffusion and hence longer runout distances and smaller deposit aspect ratios. Furthermore, entrapment of cold ambient air by falling hot pyroclastic mixtures (Trolese et al., 2019) can cause thermal pressurization within the concentrated mixtures, which can contribute to increased pore pressure (Chédeville & Roche, 2018).

In contrast to our experimental materials, pyroclastic mixtures are commonly highly polydisperse and in this respect the behavior of the finest particles can complicate the processes discussed above in two ways. First, the fraction of fine particles that could remain trapped in the concentrated mixture formed in the impact zone could decrease significantly the material permeability, which would favor higher amounts and lower diffusion rates of pore pressure. Second, as discussed by Sweeney and Valentine (2017), the remaining fraction of fine particles can be expelled with the gas from the mixture emerging from the impact zone, hence creating a dilute turbulent suspension overriding the concentrated flow and possibly moving at a higher velocity. In this regard, particle clusters with high sedimentation rates in the dilute suspension can rapidly accumulate above the concentrated basal flow to generate pore pressure and hence extend the duration of pore pressure diffusion in the mixture (Breard et al., 2018; Penlou, Roche, Manga, et al., 2023).

6. Conclusion

Our experiments show that dilute mixtures of particles with Stokes numbers of 10^{-1}–10^{1} in free-fall and impacting a rigid substrate accumulate to form granular flows with almost maximum particle concentration. The consequence of the rapid accumulation of particles in the impact zone is the creation of pore air pressure in the concentrated granular flows. In this configuration, and all other parameters being equal, the particle size controls

the mechanisms that operate upon impact and during subsequent flow emplacement. As particle size and thus material permeability decreases, the pore air pressure increases (and indicates almost full bed weight support for particle sizes ≤76 μm), and the flow runout distance increases due to higher initial pore pressure and slower pressure diffusion. This study suggests that concentrated PDCs with high pore pressure can emerge from the impact zone of eruptive fountains and that at given initial conditions finer mean grain size can promote longer runout distances of the currents. The mechanisms observed in experiments are expected to occur more efficiently in nature owing to mean particle sizes of same order, higher impact velocities and thicker flow thicknesses. However, several properties of the natural mixtures were not taken into account in our experiments. These include particle size polydispersity, very low particle concentrations (≪1 vol.%), supersonic and thermal effects, and slope angle of the impact zone. Further investigation is needed to understand the influence of these parameters.

Data Availability Statement

The data and associated descriptions [Dataset] in this paper are available at (Penlou, Roche, van den, & Wildenberg, 2023).

Acknowledgments
This project is part of a program of the International Research Center of Disaster sciences and sustainable Development at University Clermont Auvergne. This is Laboratory of Excellence ClerVolc contribution no 633. We thank Michael Manga for stimulating discussions on an earlier draft. Detailed comments from Greg Valentine, Pete Rowley and an anonymous reviewers helped improve the manuscript.

References

Anderson, T., & Flett, J. S. (1903). Report on the eruptions of the soufrière, St. Vincent, and on a visit to Montagne Pelèe. In *Martinique.—Part I. Philosophical transactions of the royal society of London. Series A, containing papers of a mathematical or physical character* (Vol. 200, pp. 353–553). https://doi.org/10.1098/rsta.1903.0010

Andrews, B. J., & Manga, M. (2012). Experimental study of turbulence, sedimentation, and coignimbrite mass partitioning in dilute pyroclastic density currents. *Journal of Volcanology and Geothermal Research*, *225–226*, 30–44. https://doi.org/10.1016/j.jvolgeores.2012.02.011

Breard, E. C. P., Dufek, J., & Lube, G. (2018). Enhanced mobility in concentrated pyroclastic density currents: An examination of a self-fluidization mechanism. *Geophysical Research Letters*, *45*(2), 654–664. https://doi.org/10.1002/2017GL075759

Breard, E. C. P., & Lube, G. (2017). Inside pyroclastic density currents—Uncovering the enigmatic flow structure and transport behaviour in large-scale experiments. *Earth and Planetary Science Letters*, *458*, 22–36. https://doi.org/10.1016/j.epsl.2016.10.016

Burgisser, A., Bergantz, G., & Breidenthal, R. (2005). Addressing complexity in laboratory experiments: The scaling of dilute multiphase flows in magmatic systems. *Journal of Volcanology and Geothermal Research*, *141*(3–4), 245–265. https://doi.org/10.1016/j.jvolgeores.2004.11.001

Cas, R. A. F., Wright, H. M. N., Folkes, C. B., Lesti, C., Porreca, M., Giordano, G., & Viramonte, J. G. (2011). The flow dynamics of an extremely large volume pyroclastic flow, the 2.08-Ma Cerro Galán Ignimbrite, NW Argentina, and comparison with other flow types. *Bulletin of Volcanology*, *73*(10), 1583–1609. https://doi.org/10.1007/s00445-011-0564-y

Chédeville, C., & Roche, O. (2018). Autofluidization of collapsing bed of fine particles: Implications for the emplacement of pyroclastic flows. *Journal of Volcanology and Geothermal Research*, *368*, 91–99. https://doi.org/10.1016/j.jvolgeores.2018.11.007

Dellino, P., Büttner, R., Dioguardi, F., Doronzo, D. M., Volpe, L. L., Mele, D., et al. (2010). Experimental evidence links volcanic particle characteristics to pyroclastic flow hazard. *Earth and Planetary Science Letters*, *295*(1–2), 314–320. https://doi.org/10.1016/j.epsl.2010.04.022

Dellino, P., Zimanowski, B., Büttner, R., Volpe, L. L., Mele, D., & Sulpizio, R. (2007). Large-scale experiments on the mechanics of pyroclastic flows: Design, engineering, and first results. *Journal of Geophysical Research*, *112*(B4), B04202. https://doi.org/10.1029/2006JB004313

Druitt, T. H., & Sparks, R. S. J. (1982). A proximal ignimbrite breccia facies on Santorini, Greece. *Journal of Volcanology and Geothermal Research*, *13*(1–2), 147–171. https://doi.org/10.1016/0377-0273(82)90025-7

Fries, A., Roche, O., & Carazzo, G. (2021). Granular mixture deflation and generation of pore fluid pressure at the impact zone of a pyroclastic fountain: Experimental insights. *Journal of Volcanology and Geothermal Research*, *414*, 107226. https://doi.org/10.1016/j.jvolgeores.2021.107226

Gilchrist, J. T., Jellinek, A. M., Hooft, E. E. E., & Wanket, S. (2023). Submarine terraced deposits linked to periodic collapse of caldera-forming eruption columns. *Nature Geoscience*, *16*(5), 446–453. https://doi.org/10.1038/s41561-023-01160-z

Guzmán, S., Doronzo, D. M., Martí, J., & Seggiaro, R. E. (2020). Characteristics and emplacement mechanisms of the Coranzulí ignimbrites (Central Andes). *Sedimentary Geology*, *405*, 105699. https://doi.org/10.1016/j.sedgeo.2020.105699

Iverson, R. M., & Denlinger, R. P. (2001). Flow of variably fluidized granular masses across three-dimensional terrain: 1. Coulomb mixture theory. *Journal of Geophysical Research*, *106*(B1), 537–552. https://doi.org/10.1029/2000JB900329

Lube, G., Breard, E. C. P., Cronin, S. J., & Jones, J. R. (2015). Synthesizing large-scale pyroclastic flows: Experimental design, scaling, and first results from PELE. *Journal of Geophysical Research: Solid Earth*, *120*(3), 1487–1502. https://doi.org/10.1002/2014JB011666

Lube, G., Breard, E. C. P., Jones, J. R., Fullard, L., Dufek, J., Cronin, S. J., & Wang, T. (2019). Generation of air lubrication within pyroclastic density currents. *Nature Geoscience*, *12*(5), 381–386. https://doi.org/10.1038/s41561-019-0338-2

McTaggart, K. C. (1960). The mobility of Nuees ardentes. *American Journal of Science*, *258*(5), 362–382. https://doi.org/10.2475/ajs.258.5.369

Pacheco-Hoyos, J. G., Aguirre-Díaz, G. J., & Davila-Harris, P. (2018). Boiling-over dense pyroclastic density currents during the formation of the ~100 km^3 Huichapan ignimbrite in Central Mexico: Stratigraphic and lithofacies analysis. *Journal of Volcanology and Geothermal Research*, *349*, 268–282. https://doi.org/10.1016/j.jvolgeores.2017.11.007

Penlou, B., Roche, O., Manga, M., & van den Wildenberg, S. (2023). Experimental measurement of enhanced and hindered particle settling in turbulent gas-particle suspensions, and geophysical implications. *Journal of Geophysical Research: Solid Earth*, *128*(3), e2022JB025809. https://doi.org/10.1029/2022JB025809

Penlou, B., Roche, O., & van den Wildenberg, S. (2023). Experimental study of the generation of pore gas pressure in pyroclastic density currents resulting from eruptive fountain collapse [Dataset]. Journal of Geophysical Research: Solid Earth. https://doi.org/10.25519/4EGC-N945

Rhodes, M. (2008). *Introduction to particle technology* (2nd ed.). John Wiley and Sons Ltd. https://doi.org/10.1002/9780470727102

Roche, O., Buesch, D. C., & Valentine, G. A. (2016). Slow-moving and far-travelled dense pyroclastic flows during the peach spring super-eruption. *Nature Communications*, *7*(1), 10890. https://doi.org/10.1038/ncomms10890

Roche, O., Henry, C. D., Azzaoui, N., & Guillin, A. (2022). Long-runout pyroclastic density currents: Analysis and implications. *Geology*, *50*(10), 1172–1176. https://doi.org/10.1130/G50215.1

Rowley, P. J., Roche, O., Druitt, T. H., & Cas, R. A. F. (2014). Experimental study of dense pyroclastic density currents using sustained, gas-fluidized granular flows. *Bulletin of Volcanology*, *76*(9), 855. https://doi.org/10.1007/s00445-014-0855-1

Schneider, C. A., Rasband, W. S., & Eliceiri, K. W. (2012). NIH image to ImageJ: 25 years of image analysis. *Nature Methods*, *9*(7), 671–675. https://doi.org/10.1038/nmeth.2089

Sparks, R. S. J., Wilson, L., & Hulme, G. (1978). Theoretical modeling of the generation, movement, and emplacement of pyroclastic flows by column collapse. *Journal of Geophysical Research*, *83*(B4), 1727–1739. https://doi.org/10.1029/JB083iB04p01727

Sweeney, M. R., & Valentine, G. A. (2017). Impact zone dynamics of dilute mono- and polydisperse jets and their implications for the initial conditions of pyroclastic density currents. *Physics of Fluids*, *29*(9), 093304. https://doi.org/10.1063/1.5004197

Trolese, M., Cerminara, M., Esposti, O. T., & Giordano, G. (2019). The footprint of column collapse regimes on pyroclastic flow temperatures and plume heights. *Nature Communications*, *10*(1), 2476. https://doi.org/10.1038/s41467-019-10337-3

Valentine, G. A. (2020). Initiation of dilute and concentrated pyroclastic currents from collapsing mixtures and origin of their proximal deposits. *Bulletin of Volcanology*, *82*(2), 20. https://doi.org/10.1007/s00445-020-1366-x

Valentine, G. A., & Sweeney, M. R. (2018). Compressible flow phenomena at inception of lateral density currents fed by collapsing gas-particle mixtures. *Journal of Geophysical Research: Solid Earth*, *123*(2), 1286–1302. https://doi.org/10.1002/2017JB015129

Valverde, J. M., & Soria-Hoyo, C. (2015). Vibration-induced dynamical weakening of pyroclastic flows: Insights from rotating drum experiments. *Journal of Geophysical Research: Solid Earth*, *120*(9), 6182–6190. https://doi.org/10.1002/2015JB012317

Wilson, C. J. N. (1980). The role of fluidization in the emplacement of pyroclastic flows: An experimental approach. *Journal of Volcanology and Geothermal Research*, *8*(2–4), 231–249. https://doi.org/10.1016/0377-0273(80)90106-7

References From the Supporting Information

Leibrandt, S., & Pennec, J.-L. L. (2015). Towards fast and routine analyses of volcanic ash morphometry for eruption surveillance applications. *Journal of Volcanology and Geothermal Research*, *297*, 11–27. https://doi.org/10.1016/j.jvolgeores.2015.03.014